Proceedings of the ASME 2022
International Design Engineering Technical Conferences & Computers and Information in Engineering Conference
IDETC/CIE 2022
August 14-17, 2021, St. Louis, Missouri

IDETC/CIE 2022- 89934

USING COAXIAL MELT POOL MONITORING IMAGES TO ESTIMATE COOLING RATE FOR POWDER BED FUSION ADDITIVE MANUFACTURING

Zhuo Yang[1, 2], Brandon Lane[3], Yan Lu[3, *], Ho Yeung[3], Jaehyuk Kim[2], Yande Ndiaye[2], Sundar Krishnamurty[4]

[1]Georgetown University, Washington, DC
[2]Associate at National Institute of Standards and Technology, Gaithersburg, MD
[3]National Institute of Standards and Technology, Gaithersburg, MD
[4]University of Massachusetts Amherst, Amherst, MA

ABSTRACT

Cooling rate is a decisive index to characterize melt pool solidification and determine local microstructure formation in metal powder bed fusion processes. Traditional methods to estimate the cooling rate include in-situ temperature measurement and thermal simulation. However, these methods may not be accurate or efficient enough under complex conditions in real-time. This paper proposes a method to approximate the melt pool cooling rate using temperature profile acquired via thermally-calibrated melt pool camera, and based on continuous pixel tracking result. The proposed method can estimate the temperature and associated cooling rate for every pixel immediately, which is potentially applicable for real-time process monitoring. This paper focuses on investigating image data processing, method development, and cooling condition analysis. This work presents the preliminary result of the cooling rate estimation under different conditions such as position, layer number, and overhanging.

Keywords: Cooling rate, additive manufacturing, powder bed fusion, in-situ monitoring, coaxial melt pool monitoring

1. INTRODUCTION

Metal Additive Manufacturing (AM) enables the fabrication of parts with complex geometry and functional gradient material properties [1]. In contrast to traditional subtractive manufacturing methods, AM creates parts layer by layer that expands the options and space for design freedom [2]. During this process, for example, a laser powder bed fusion (LPBF) AM machine repeatedly uses a focused laser beam to melt and remelt powder material. Metal material on the build platform could undergo multiple times of melting and solidification cycles. The thermal condition history is a key to the fabricated part quality; and controlling material thermal dynamics is an ongoing area of research and development. Ideally, thermal sensors, such as thermal imagers or pyrometers, could provide direct temperature measurement. However, these sensors may not always available, or may not be able to resolve the spatial and temporal dynamic characteristics of LPBF. This paper presents an alternative cooling rate estimation approach based on melt pool monitoring (MPM) images that are captured by a high-speed coaxial camera. Temperature profiles are created from the time series images for individual pixels and fit with a cooling rate model.

A core goal of AM process monitoring research is to attempt to build a correlation between in-process signatures to final AM part qualities, so that the quality may be predicted a-priori during the build. Spatial and temporal thermal conditions during the build compose a set of critical signatures that can be used to detect the anomaly initiation such as residual heat and lack of fusion [3,4]. Keyholing, which is another potentially harmful phenomena, can create porosity in the part. This observation is believed to associate with the overheating and can be identified from melt pool temperature [5].

Keyholing or overheating may be predicted using monitored machine values such as galvo position and laser power, which determines the input energy density [6]. However, previous findings indicate the same energy input does not always result in the same size or temperature of the melt pool [7]. Different boundary conditions from the part geometry, scan history, material, or environment can affect the transient thermal dynamics. For example, the thermal conductivity of raw powder and solidified material can be very different [8,9].

Cooling rate may be a key signature to investigate the solidification process, which directly relate to final part structure. For example, when laser re-scans a previously melted region, the instantaneous solid or liquid phase of that region determines whether this region is remelted, or the molten melt pool fuses with itself to effectively form a larger melt pool [10]. It is hard to verify the abovementioned conditions without knowing the temperature of the melt pool. It is necessary to develop a method which can accurately calculate the melt pool temperature. If applied to real-time control, the method cannot be computational costly.

Coaxial monitoring utilizes optical beam splitters in the path of the laser to separate the laser wavelength from optical emissions from the melt pool [11]. This enables the melt pool to continually remain in the field of view of the monitoring sensor or camera throughout the build process. Various examples exist of coaxial melt pool imaging and in-situ temperature measurement methods [12-14]. Only a few examples of them are about thermally-calibrated coaxial melt pool imaging, where each pixel in the image can be ascribed a related temperature value [15]. However, doing so provides the advantages of coaxial imaging (e.g., continuous monitoring that covers the entirety of the build plane resolved at micrometer scale [16]), and of course, temperature-related signatures to characterize with key phenomena such as material solidification.

Current methods that provide the surface temperature of the melt pool includes simulation and direct measurement. Finite element analysis (FEA) and computational fluid dynamic (CFD) methods can estimate the temperature based on scan path and thermal input [17,18]. These physics-based approaches usually request long computational time that can be difficulty applied in real-time [19]. Thermal imaging is another way to measure the surface temperature. However, the dynamic range of the camera may not observe all the wide range of temperatures [20]. All these situations push the research to deliver an affordable method to provide the surface temperature of the melt pool.

This paper aims to develop a cooling rate model that enables estimating the temperature profile of the melt pool using coaxial melt pool imaging. Section 2 introduces the general workflow of tracking melt pool changes from series MPM frames and fitting cooling rate model from optical signals. Section 3 details the experimental design and data statistics. Section 4 presents the results of modeling and application. Section 5 has a brief summary and demonstrates how this method is used to analyze cooling rate under different build conditions.

2. MOTIVATION AND METHOD DEVELOPMENT

2.1 Motivation

The authors' previous work made a lot of effort in analyzing the optical melt pool images for anomaly detection, quality control, predictive modeling, and process optimization [21-24]. The raw images provide value to process monitoring by capturing optical signal of the melt pool in micro-meter/second scale [25]. However, the raw images have intrinsic limitation in that the pixel values do not directly represent a temperature measurement. A recent study from the co-authors breaks this barrier by calibrating the camera raw signal to radiance temperature using a custom light-emitting diode (LED) based thermal calibration source within the same LPBF testbed the laser-scanning experiments are conducted [26]. The progress encourages the authors to attempt a method to estimate the melt pool temperature against the time from optical MPM images. The 8 µm image resolution and 10,000 Hz frame rate meet the requirement for real-time monitoring.

2.2 Fundamental Approach

The fundamental idea of the proposed method is to track the temperature at the same location on the build plate from multiple continuous MPM frames. The first step is to build the correlation between individual MPM frame, without position and temporal information, to the machine coordinate system. Melt pool superimposition is a technique to accurately assign every pixel of the MPM image to the machine coordinate system based on data alignment and signal synchronization [Yeung et al, 2021]. Other terms such as AM data registration or data fusion utilize the same technique to extend the usage of superimposed melt pool data [27]. Details of related techniques can be found in the authors' previous publications. The following content will limit the topics on cooling rate approximation and compare the differences under various conditions.

Fitting the cooling rate using real MPM images requires two main steps. The first step is to build a complete pixel tracking history from continuous MPM frames. The tracking history denotes to record the value changes over the time of the pixels. This step relies on the truth that a position on the build plate can be covered by several continuous frames. Increasing the frame size and sampling rate or decreasing the scan speed can yield longer or more frequent tracking history. The second step is to fit the cooling rate model based on temperature-time tracking data of each overlapping or superimposed position. According to the thermal theory, this model will be monotonically decreasing, though noise may add some variance to the timeline.

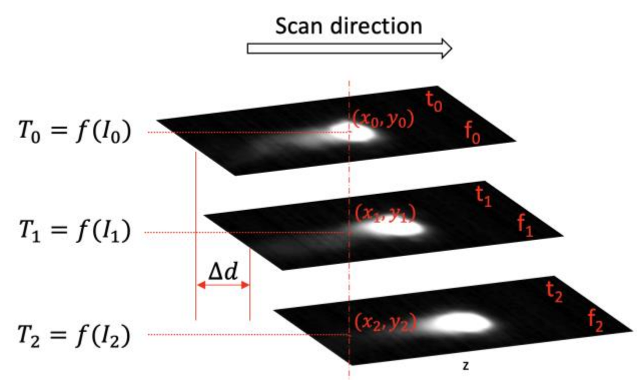

Figure 1. Graphical representation of the pixel tracking method

Figure 1 shows the graphical representation of the pixel tracking history from 3 consecutive MPM frames. The frame on the top row superimposes a melt pool at the initial state. In this example, the selected pixel locates at (x_0, y_0) on the frame coordinate system. The labels f_0 and t_0 represent Frame 0 at Time 0. The initial temperature T_0 is calculated based on initial optical signal I_0. This study utilizes the Sakuma-Hattori equation as a regression model f to relate camera signal I to the temperature T based on the thermal calibration results [28]. The middle and bottom frames are the second and last times that captured the value of the same position. The laser scan direction is from left to right. While deploying constant scan speed and fixed frame rate, the distance between the two frames is fixed to Δd. The dashed line indicates the three different pixels on those frames actually point to the same position to the machine coordinate system.

2.3 Build Pixel Tracking History

The pseudocode of building the tracking history of all pixels in one melt pool is shown below:

1. Represent the raw 120×120 MPM frame at $t = t_0$ in linear indices (All pixels $A_{t_0} = \{p_{t_0}^1, p_{t_0}^2 \dots p_{t_0}^{14400}\}$)
2. Select saturated pixels $S_{t_0} = \{p_{t_0}^j, p_{t_0}^{j+1} \dots p_{t_0}^n\}$ (8-bit grayscale level 255) and create a mask
3. Calculate the pixel temperature from grayscale using calibrated Sakuma-Hattori equation, excluding pixels under the threshold (to eliminate low intensity and noisy pixels)
4. Save temperature of each pixel to profile $\{T_{t_0}^j\}$
5. Find the position of same pixel S_{t_0} in next MPM frame, where $t = t_0 + \Delta t$
6. If any S_{t_0} can be located on the new frame:

    5.1 Add T_t^j to the temperature profile

    5.2 Repeat Step 4

    Else:

    5.3 Stop

2.4 Approximate the Cooling Rate

After investigating all interested MPM frames, the tracking history can create a dataset with a complete temperature-time profile. However, conditions such as pixel position can affect the pixel tracking length. Usually, a longer time window, higher frequency, and larger frame size can include more melt pool thermal historical information. Higher data quality can thus reduce the model uncertainty. The longest tracking time depends on the maximum number of frames covering the same position without reducing the scan speed. One way to improve this condition is to increase the sampling rate and enlarge the field view of the camera. However, simply elevating these numbers may result in poor exposure and low resolution. A suitable model should balance these features other than simply adding more low-quality training data. Section 4 will investigate the modeling difference under different conditions in both data and physical perspectives.

The following matrix shows the data structure of the temperature-time history of the pixels for cooling rate modeling. In this matrix, the rows are the pixel number, and the columns are the time. The element represents the temperature at timepoint i for pixel j. According to pixel position and frame size, the trackable time can differ from pixel to pixel. For pixels that cannot be tracked at a certain moment, the element has no value in the matrix and will not be included in the model fitting.

$$\begin{array}{c c} & \begin{array}{cccc} \boldsymbol{t_0} & \boldsymbol{t_1} & & \boldsymbol{t_j} \end{array} \\ \begin{array}{c} \boldsymbol{P^1} \\ \boldsymbol{P^2} \\ \\ \boldsymbol{P^i} \end{array} & \begin{bmatrix} T_0^1 & T_1^1 & \cdots & T_j^1 \\ T_0^2 & T_1^2 & & T_j^2 \\ \vdots & & \ddots & \vdots \\ T_0^i & T_1^i & \cdots & T_j^i \end{bmatrix} \end{array}$$

The cooling rate model deploys two-term exponential regression model to fit the temperature and time based on Newton's law of cooling.

$$T = (T_0 - a)e^{b\Delta t} + a \tag{1}$$

Where T is the estimated temperature, T_0 is the initial temperature, Δt is time difference, and a and b are the two coefficients.

2.5 Pixel Selection

Generally, any trackable pixel on the MPM frame can be used to build the temperature profile. This section discusses the different pixel selection methods and the potential impact on the estimated cooling rate. The main idea is to select only those pixels with the same initial temperature and the most extended tracking history. The tracking begins with the pixels with the highest initial temperature to achieve the first goal. The saturated pixels would be the ideal starting point for building the temperature profile when referring to the original grayscale value. In that case, grayscale level 255 for 8-bit unsigned integer (uint8) would be a uniform start point for data points. The second goal can guarantee enough samples to fit the cooling rate model over time. For example, a pixel near the image edge will soon move out of the tracking window. It is too short to fit a cooling rate model for less than 3 data points. Combining with the two goals, the center of the melt pool, whose grayscale value is saturated at 255 (uint8), seems to be the ideal solution.

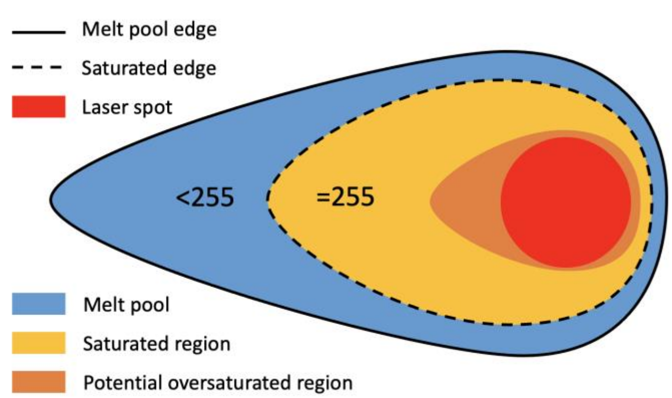

Figure 2. Grayscale distribution of the melt pool.

However, the saturated region of the melt pool is also the active region of the laser beam. Thus, the heat source directly working on that region can exceed the camera limitation. On the other hand, it indicates that pixels with the same grayscale value may have different temperatures obscured by the saturation. The unsaturated pixels closer to the laser spot likely have higher thermal gradients and MPM pixel values. This condition can produce false initial temperature values that further impact the cooling rate estimation. This research proposes three selection methods to investigate the differences in tracking options and deliveries.

Figure 2 demonstrates the conceptual melt pool captured by the MPM image. 255 is the highest grayscale value derived from the optical signal. However, temperature over this threshold would not provide a higher grayscale value. Thus, the melt pool can be divided into four regions. The laser spot has the highest energy density. Though the entire saturated region (yellow) has the same grayscale value of 255, the orange region is more likely to be oversaturated since it is closer to the laser spot. The longer the distance from the laser spot, the lower the chance of oversaturated measurement. The grayscale value of the blue region is less than 255, which may accurately reflect the pixel temperature. The solid line is the melt pool outline, which is determined by the melting temperature. The dashed line marks the margin of saturated and non-saturated regions. The pixels on the margin are least likely to be oversaturated.

To identify the potential oversaturation impact, the research selects the pixels on three regions: 1) all saturated pixels in the melt pool; 2) saturated pixels on the front of the melt pool nearest the laser spot; 3) saturated pixels nearer the rear of the melt pool.

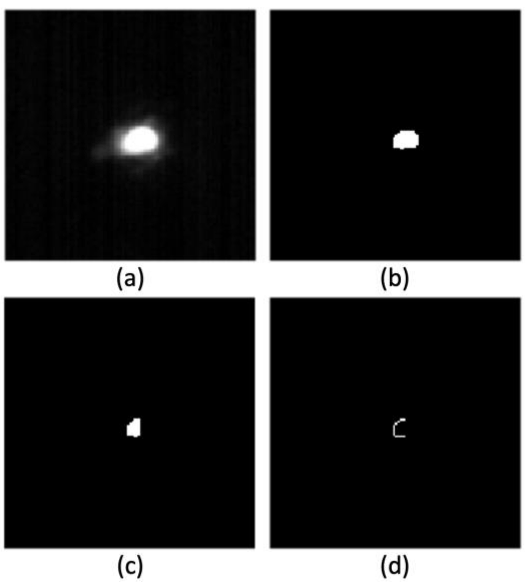

Figure 3. Comparison of different pixel selection method. (a) is the original MPM image. (b) shows all saturated pixels. (c) is (b) after remove the pixels close to the laser spot. (d) shows the saturated pixels on the melt pool edge near the tail.

Figure 3 shows the raw MPM image (a) and the pixels selected by different methods. (b) selects all the pixels whose grayscale value is equal to 255. (c) filters out the pixels close to the laser spot, where those pixels are likely to be oversaturated. (d) further removes more pixels and only maintains those on the outline near the melt pool tail. Those pixels are assumed to be the marginal pixels that would effectively have values slightly above 255 if they were not saturated. Note that the last method automatically removes the pixels on the front edge since they may be entering the heating process during the laser scanning.

Figure 4 shows the tracking history for a set of pixels in one melt pool. For the demonstrative purpose, this figure plots the initial grayscale of the tracking pixel from Frame 1 to Frame 7. The process tracks 96 saturated pixels starting at 255. There are 28 pixels out of tracking after 6 frames. Original Frame 1 to 3 are shown on the top. The red spot marks one tracking pixel captured at different time.

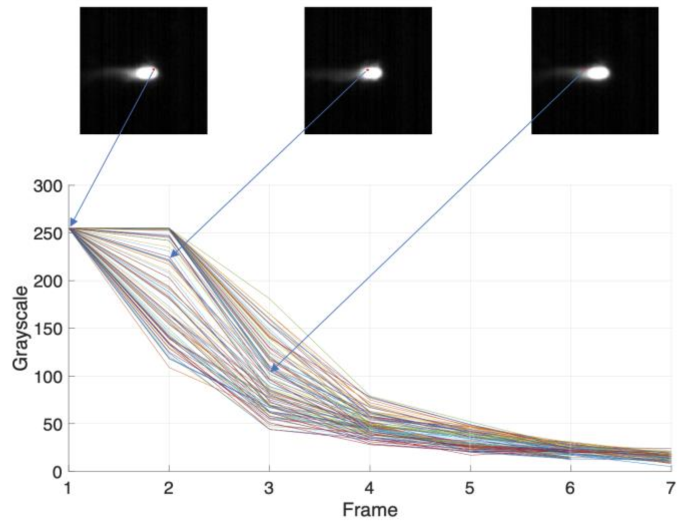

Figure 4. Tracking history (grayscale-frame) for a set of pixels of one melt pool. Colored lines represent the grayscale value of individual pixel on each frame. This example selects one pixel to show its track in three frames.

3. EXPERIMENT AND DATA

3.1 AMMT

The Additive Manufacturing Metrology Testbed (AMMT) at the National Institute of Standards and Technology (NIST) is the primary platform developed to study powder bed fusion processes. AMMT is a fully customized metrology instrument that enables flexible control and measurement of the L-PBF process [16]. It is equipped with the capability of precise laser beam control and high-rate in-situ monitoring, including a coaxial camera for melt pool imaging. Using custom-developed scan strategy design software, the digital commands that AMMT uses set precise laser beam position and laser beam power at 100 KHz, and synchronously triggers the MPM camera every 100 µs (or 10 KHz) [29]. This provide a way to superimpose the MPM to the position, so it is easy to track the pixels.

3.2 Experiment

For this study, an experiment is designed to create parts with multiple features such as scan direction, overhang, and varying laser power. This experiment creates four nominally identical parts within the same build on a wrought nickel alloy 625 (IN625) substrate cut to 100 mm x 100 mm x 12.5 mm. All four parts have the same geometry: a bounding box 5 mm x 9 mm x

5 mm, a 45° overhang feature and a cylinder cavity. Later result of overhang cooling rate is based on the MPM frames on cylinder cavity. The powder material is mixture of recycled and virgin IN625 powder. The build consists of 250 layers at 20 µm per layer. The build employs a constant speed (800 mm/s) constant power (195 W) stripe scan pattern with skywriting for infilling area. Pre-contour scan uses laser power 100 W. The MPM frames of pre-contour are used to fit the cooling rate of low laser input. Detailed experiment descriptions can be found in Ly et al, 2017 [30]. The general scan direction is designed to rotate 90° every layer. Next session also fits cooling for opposite directions.

3.3 Data

Each layer, according to the scan patten and infilling area, collects 5000 to 6000 MPM frames using constant camera settings for frequency and exposure time. The frame rate for this experiment is set to 10,000 kHz (100 µs/frame). MPM is 120 pixels × 120 pixels where each pixel is 8 µm × 8 µm. That gives each frame a 0.96 mm × 0.96 mm rectangular monitoring region. The 800 mm/s scan speed is equal to 10 pixels per 100 µs. Combining everything together, one pixel location can have up to 7 frames covering. On the other hand, the tracking history is constructed by 7 data points for each pixel, spanning 700 µs.

4 RESULTS

This section presents the preliminary result for the fitted cooling rate under different circumstances. Each circumstance has identical tracking history since the MPM frames are different. Section 4.1 compares the cooling rate models of the three tracking methods fitted by the same dataset. Section 4.2 presents a more detailed comparison of 11 tracking groups under different conditions.

The Sakuma-Hattori equation for calculating the temperature is adopted from the calibration result on the same testbed [28].

$$T_{app}(I) = \frac{c_2}{a\,ln(\frac{c_1}{I}-1)} - \frac{b}{a} - 273.15 \qquad (2)$$

Where the fitted coefficients a = 0.2971, b = 464.2328, c_1=5.1201e+07, and the second radiation constant c_2=14338 µm/K.

4.1 Fitting Cooling Rate by Different Tracking Method

This section builds the tracking history from one continuous scan with 112 MPM frames. 1300 saturated pixels construct the initial status. To avoid repeated pixels, 16 frames were selected as the starting points. The initial temperature T_0 is 2117 °C calculated from Equation (1). Figure 5 shows the measured data and fitted cooling rate model. The fitted cooling rate model is shown in Equation (3). The final tracking history is built from 1301 pixels.

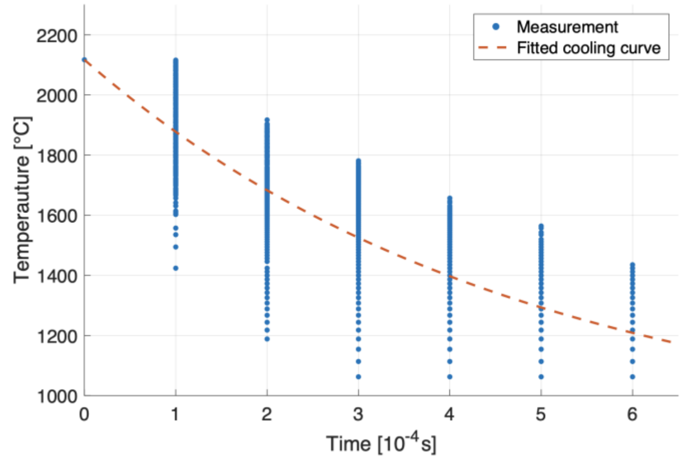

Figure 5. Cooling rate curve fitted by all saturated pixels. Data points are the temperature of all tracking pixels for each timestep.

$$T = (T_0 - 845.8421)e^{-0.0203\Delta t} + 845.8421 \qquad (3)$$

Data without the pixels close to the laser spot fit a different cooling rate. Figure 6 shows the cooling rate fitted by only the pixels far from the laser spot. The model is shown in Equation (4). It involves fewer pixels to fit the model. Finally, the model investigates a total of 727 pixels.

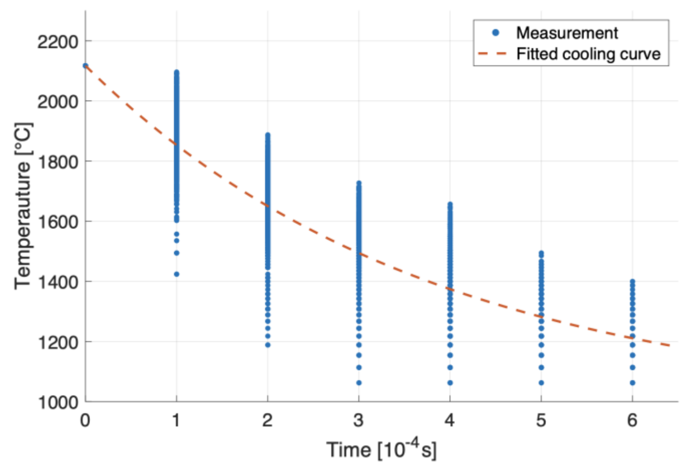

Figure 6. Cooling rate curve fitted by saturated pixels far from the laser spot.

$$T = (T_0 - 974.6053)e^{-0.0263\Delta t} + 974.6053 \qquad (4)$$

The last cooling rate model uses the least amount of pixel tracking history. Only 252 pixels were survived. 80% of the pixels not on the melt pool edge were eliminated. Equation (5) is the result, where the plot is shown in Figure 7.

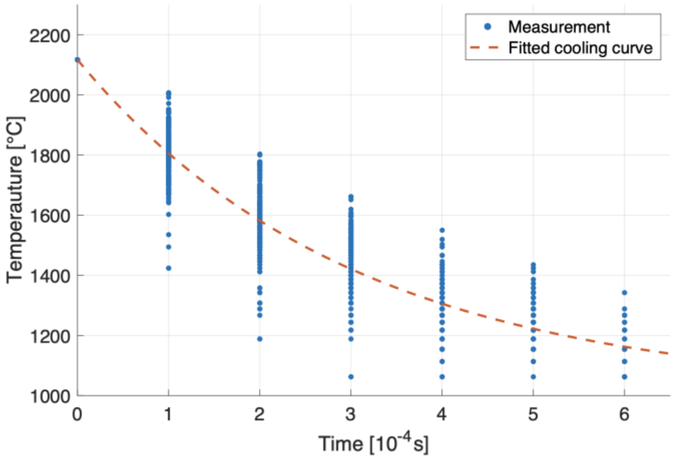

Figure 7. Cooling rate curve fitted by the pixels on the melt pool edge.

$$T = (T_0 - 1010.1550)e^{-0.0330\Delta t} + 1010.1550 \quad (5)$$

Figure 8 plots the three cooling rate curves. The comparison shows that the cooling rate is steeper after removing more potential oversaturated pixels. Saturated pixels display lower temperatures than what is real. This can be the reason that makes the curve moderate.

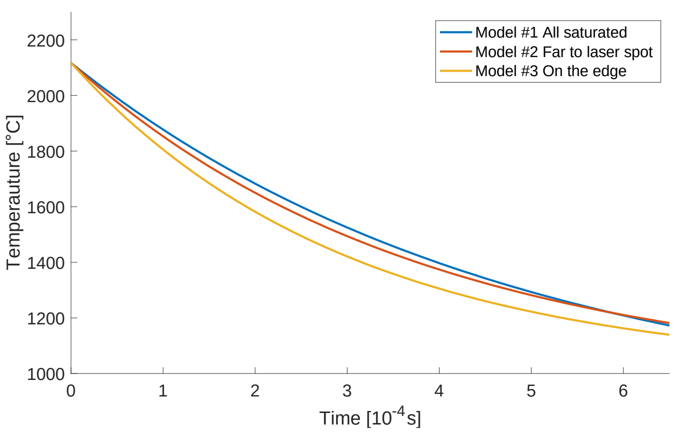

Figure 8. Comparison of the cooling rate models fitted from different tracking methods.

4.2 Cooling Rate Comparison under Multiple Conditions

Ideally, the cooling rate should be consistent for the same material under similar conditions. This section compares 14 tracking groups with unique characteristics. Each group tracks only corresponding MPM frames. Unless explicitly stated, most groups scan horizontally from left to right using 195W laser power (Table *1*). Group 1 to 3 are three tracks from the same layer at early, middle, and late time to investigate the cooling rate changes within one layer. Groups 4 to 6 divide MPM frames from the same melting track into three sub-groups: beginning, middle, and end. It aims to compare the cooling rate changes in one continuous melting track. Group 7 to 9 have different scan directions. Group 10 to 12 are the tracks at the same location but different layers. Group 13 is the MPM frames on the pre-contour that laser power equal to 100W. Group 14 tracks the frames located on the overhang region. The previous study shows that overhang can significantly affect the melt pool formation without solid support underneath [31].

Table 1. Tracking groups with unique characteristics.

	Characteristic	Layer	Sample size
1	Early-track	2	112
2	Mid-track	2	112
3	Late-track	2	112
4	Beginning of one track	2	30
5	Middle of one track	2	30
6	End of one track	2	30
7	Horizontal right to left	2	112
8	Vertical bottom to top	3	61
9	Vertical top to bottom	3	61
10	Layer 50	50	105
11	Layer 150	150	105
12	Layer 250	250	105
13	Pre-contour (100W)	2	100
14	Overhang	226	30

Figure 9 annotates the groups on Layer 2. Arrows represent the beam moving direction. The scan starts from the top and uses horizontal skywriting to the bottom after the pre-contour. This layer collects a total of 5969 MPM frames.

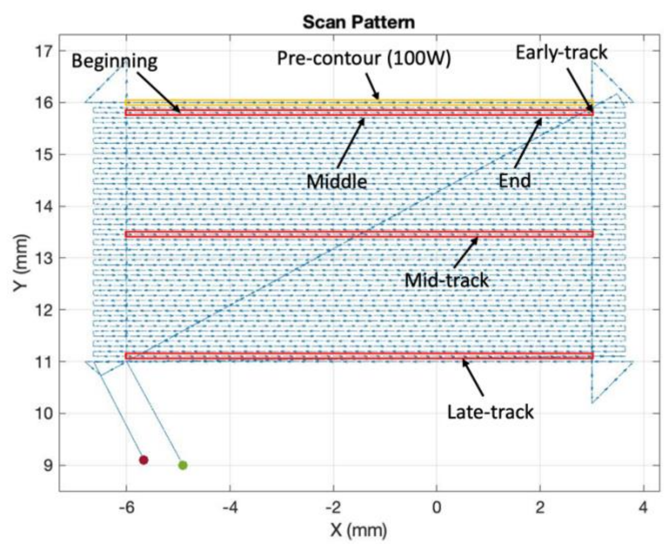

Figure 9. Scan pattern and frame tracking positions of Layer 2. Arrow represents the laser scan direction. Yellow and red blocks mark the MPM frames positions.

Figure 10 shows the result of the 14 groups listed in Table 1. In general, the cooling rate for most groups does not exhibit significant differences. Black curves of Groups 4 to 6 are close to each other. However, the cooling rate is gradually decreased from Group 1 to Group 3. Similarly, scan direction also affects the cooling rate where Group 9 is clearly lower than Group 7. Group 10 to Group 12 shows that the layer number can change the cooling rate. This may be correlated to geometry and building time. It is no surprise that the pre-contour group has the fastest temperature drop since the laser power is as low as 100W. Group 14, overhang, has the highest temperature after 600µs. This can be caused by the entirely different boundary conditions in heat transfer.

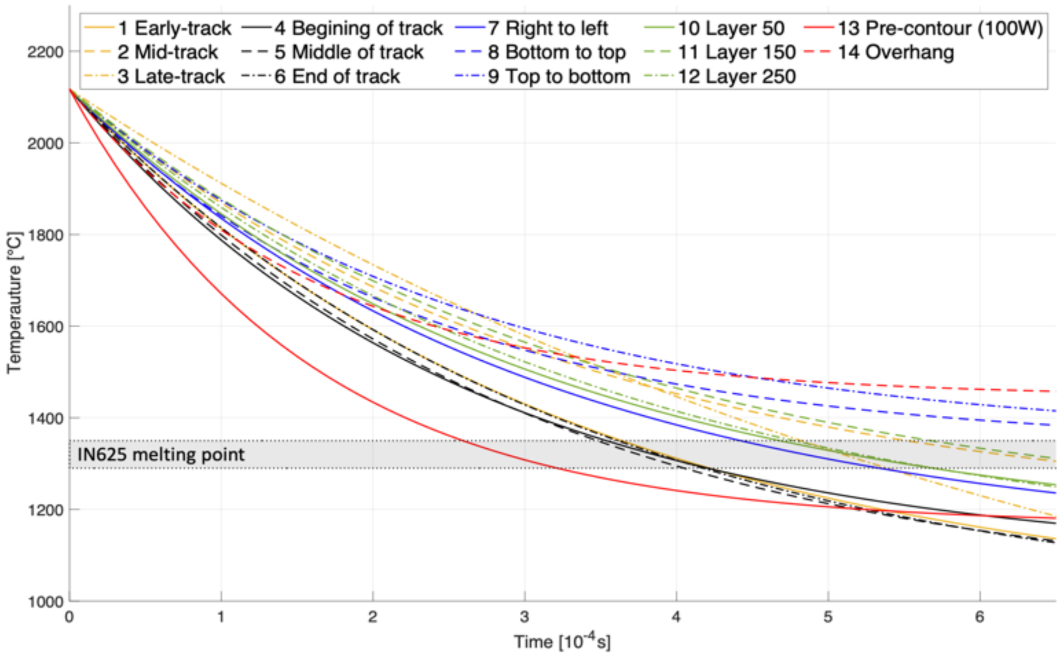

Figure 10. Cooling rate comparison of the 14 unique groups. Gray region is the melting point of IN625.

Note, all result presented in this section is based on edge tracking method. Additionally, Table 2 lists the coefficients of the fitted model for each group.

Table 2. Coefficients of fitted cooling rate model, Equation (1)

	a	b
1	988.4643	-0.0313
2	1177.3986	-0.0307
3	578.6046	-0.0143
4	1084.5639	-0.0384
5	1008.2871	-0.0338
6	970.0933	-0.0306
7	1121.0911	-0.0333
8	1338.6911	-0.0438
9	1350.4726	-0.0381
10	1165.3002	-0.0633
11	1444.9482	-0.0610
12	1133.9792	-0.0324
13	1094.8711	-0.0291

5 DISCUSSION

The proposed method is a new attempt to use the MPM image sensor data to approximate the cooling rate on the micrometer level. The paper shows the promising result and potential application of real-time monitoring and control. However, future research needs to collect additional evidence to verify the result physically. For example, the method can be more convincible if infrared camera data can provide an additional in-situ temperature measurement during the build. Moreover, future research should compare the cooling rate under other conditions such as scan direction, powder material, and overhang intensity.

The authors also noticed the potential applications of this method in AM data fusion [31]. The temperature profile of individual melt pool from the cooling rate model can extend to layer and part level. Estimation of the layerwise temperature profile is possible, potentially analyzing the residual heat and verifying the thermal simulation models [28].

Figure 11 shows the temperature change of the melt pool estimated from the cooling rate models. The melting point of IN625 is between 1250°C to 1390°C [28]. All models predict that 600 -700 µs is enough to solidify the melt pool completely. This information helps analyze the part's remelting conditions [32]. If laser beam revisits an area while still melting, the newly created melt pool is more likely to fuse the liquid metal together, resulting in an over-fusion issue. However, the situation would be different if the laser revisit occurs while the previous melt pool completely cools down. Instead of fusion, remelting happens and binds the AM part together.

6 SUMMARY

This study develops a method to estimate cooling rate by tracking pixels in MPM frames. The method requests no additional cost for the AM machines equipped with coaxial melt pool cameras. The only prerequisite is the calibration from an optical signal to temperature. This is important to capture the correct temperature-time information for fitting the cooling rate coefficients.

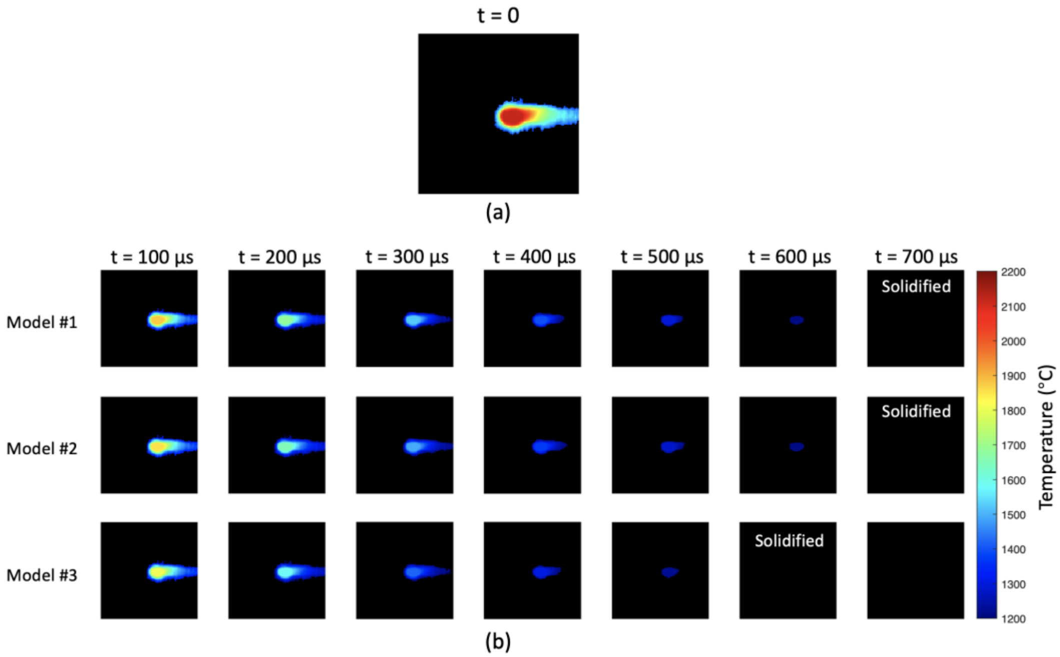

Figure 11. Temperature profile of the melt pool based on three tracking methods. (a) is the original temperature distribution calculated from raw MPM image. The cooling rate models estimate the temperature change over the time. They show the melt pool tend to solidify after 600 μs.

In general, fitting the cooling rate using this method is fast and reliable. There is no statistical violation against thermal physics. Another advantage of this method is that the fitted cooling rate model can estimate the temperature profile with the exact resolution as an MPM image. This is important since the detailed temperature profile of the melt pool can potentially contribute to many in-situ process analyses and real-time control utilities.

The article also presents the investigation of the cooling rate under different conditions. Based on the preliminary result, pixels on the melt pool edge can remove most oversaturated pixels. It also shows the contour scan using lower laser power yields the steepest temperature decrease of the pre-contour melt pool. On the other hand, the melt pool on the overhang region tends to maintain the temperature above the melting point longer than any other situation. The findings indicate that the energy input and boundary conditions can be critical factors to affect the melt pool cooling rate. Future work would focus on developing new experiment to verify the fitted cooling model based on the same material and process parameters.

DISCLAIMER

Certain commercial systems are identified in this paper. Such identification does not imply recommendation or endorsement by NIST; nor does it imply that the products identified are necessarily the best available for the purpose. Further, any opinions, findings, conclusions, or recommendations expressed in this material are those of the authors and do not necessarily reflect the views of NIST or any other supporting U.S. government or corporate organizations.

ACKNOWLEDGMENTS

This material is based upon work supported by the National Institute of Standards and Technology (NIST) under Cooperative Agreement number NIST 70NANB18H258.

REFERENCES

[1] Loh, Giselle Hsiang, Eujin Pei, David Harrison, and Mario D. Monzón. "An overview of functionally graded additive manufacturing." Additive Manufacturing 23 (2018): 34-44.

[2] Zhang, C., Chen, F., Huang, Z., Jia, M., Chen, G., Ye, Y., ... & Lavernia, E. J. (2019). Additive manufacturing of functionally graded materials: A review. Materials Science and Engineering: A, 764, 138209.

[3] Gong, Haijun, Khalid Rafi, Hengfeng Gu, Thomas Starr, and Brent Stucker. "Analysis of defect generation in Ti–6Al–4V parts made using powder bed fusion additive manufacturing processes." Additive Manufacturing 1 (2014): 87-98.

[4] Malekipour, Ehsan, and Hazim El-Mounayri. "Common defects and contributing parameters in powder bed fusion AM process and their classification for online monitoring and control: a review." The International Journal of Advanced Manufacturing Technology 95, no. 1 (2018): 527-550.

[5] Bayat, Mohamad, Aditi Thanki, Sankhya Mohanty, Ann Witvrouw, Shoufeng Yang, Jesper Thorborg, Niels Skat Tiedje, and Jesper Henri Hattel. "Keyhole-induced porosities in Laser-based Powder Bed Fusion (L-PBF) of Ti6Al4V: High-fidelity modelling and experimental validation." Additive Manufacturing 30 (2019): 100835.

[6] Kim, F. H., Ho Yeung, and E. J. Garboczi. "Characterizing the effects of laser control in laser powder bed fusion on near-surface pore formation via combined analysis of in-situ melt pool

monitoring and X-ray computed tomography." Additive Manufacturing 48 (2021): 102372.
[7] Jones, Kevontrez, Zhuo Yang, Ho Yeung, Paul Witherell, and Yan Lu. "Hybrid Modeling of Melt Pool Geometry in Additive Manufacturing Using Neural Networks." In International Design Engineering Technical Conferences and Computers and Information in Engineering Conference, vol. 85376, p. V002T02A031. American Society of Mechanical Engineers, 2021.
[8] Mukherjee, T., H. L. Wei, A. De, and Tarasankar DebRoy. "Heat and fluid flow in additive manufacturing—Part I: Modeling of powder bed fusion." Computational Materials Science 150 (2018): 304-313.
[9] Yan W, Lu Y, Jones K, Yang Z, Fox J, Witherell P, Wagner G, Liu WK. Data-driven characterization of thermal models for powder-bed-fusion additive manufacturing. Additive manufacturing. 2020 Dec 1;36:101503.
[10] Tang, Ming, P. Chris Pistorius, and Jack L. Beuth. "Prediction of lack-of-fusion porosity for powder bed fusion." Additive Manufacturing 14 (2017): 39-48.
[11] Berumen, S., Bechmann, F., Lindner, S., Kruth, J.-P., and Craeghs, T., 2010, "Quality Control of Laser- and Powder Bed-Based Additive Manufacturing (AM) Technologies," Physics Procedia, 5, Part B, pp. 617–622.
[12] Grasso, M., and Colosimo, B. M., 2017, "Process Defects and in Situ Monitoring Methods in Metal Powder Bed Fusion: A Review," Meas. Sci. Technol., 28(4), p. 044005.
[13] Hooper, Paul A. "Melt pool temperature and cooling rates in laser powder bed fusion." Additive Manufacturing 22 (2018): 548-559.
[14] Jeon, Ikgeun, Liu Yang, Kwangnam Ryu, and Hoon Sohn. "Online melt pool depth estimation during directed energy deposition using coaxial infrared camera, laser line scanner, and artificial neural network." Additive Manufacturing 47 (2021): 102295.
[15] Lane, B., Yeung, H., and Yang, Z., 2022, "Statistical and Spatio-Temporal Data Features in Melt Pool Monitoring of Additive Manufacturing," Proceedings of the 2022 IISE Annual Conference, Seattle, WA.
[16] Lane, Brandon, Sergey Mekhontsev, Steven Grantham, M. L. Vlasea, Justin Whiting, Ho Yeung, Jason Fox et al. "Design, developments, and results from the NIST additive manufacturing metrology testbed (AMMT)." In 2016 International Solid Freeform Fabrication Symposium. University of Texas at Austin, 2016.
[17] Ma, Li, Jeffrey Fong, Brandon Lane, Shawn Moylan, James Filliben, Alan Heckert, and Lyle Levine. "Using design of experiments in finite element modeling to identify critical variables for laser powder bed fusion." In 2014 International Solid Freeform Fabrication Symposium. University of Texas at Austin, 2015.
[18] Acharya, Ranadip, John A. Sharon, and Alexander Staroselsky. "Prediction of microstructure in laser powder bed fusion process." Acta Materialia 124 (2017): 360-371.
[19] Jones, Kevontrez, Zhuo Yang, Ho Yeung, Paul Witherell, and Yan Lu. "Hybrid Modeling of Melt Pool Geometry in Additive Manufacturing Using Neural Networks." In International Design Engineering Technical Conferences and Computers and Information in Engineering Conference, vol. 85376, p. V002T02A031. American Society of Mechanical Engineers, 2021.
[20] Gutknecht, Kai, Lukas Haferkamp, Michael Cloots, and Konrad Wegener. "Determining process stability of laser powder bed fusion using pyrometry." Procedia Cirp 95 (2020): 127-132.
[21] Yang, Zhuo, Yan Lu, Ho Yeung, and Sundar Krishnamurty. "Investigation of deep learning for real-time melt pool classification in additive manufacturing." In 2019 IEEE 15th international conference on automation science and engineering (CASE), pp. 640-647. IEEE, 2019.
[22] Yeung, Ho, Zhuo Yang, and L. Yan. "A meltpool prediction based scan strategy for powder bed fusion additive manufacturing." Additive Manufacturing 35 (2020): 101383.
[23] Yang, Zhuo, Yan Lu, Ho Yeung, and Sundar Krishnamurty. "From scan strategy to melt pool prediction: A neighboring-effect modeling method." Journal of Computing and Information Science in Engineering 20, no. 5 (2020): 051001.
[24] Moges, Tesfaye, Zhuo Yang, Kevontrez Jones, Shaw Feng, Paul Witherell, and Yan Lu. "Hybrid modeling approach for melt-pool prediction in laser powder bed fusion additive manufacturing." Journal of Computing and Information Science in Engineering 21, no. 5 (2021).
[25] Fox, Jason C., Brandon M. Lane, and Ho Yeung. "Measurement of process dynamics through coaxially aligned high speed near-infrared imaging in laser powder bed fusion additive manufacturing." In Thermosense: thermal infrared applications XXXIX, vol. 10214, pp. 34-50. SPIE, 2017.
[26] Deisenroth, D. C., Mekhontsev, S., Lane, B., Hanssen, L., Zhirnov, I., Khromchenko, V., Grantham, S., Cardenas-Garcia, D., and Donmez, A., 2021, "Measurement Uncertainty of Surface Temperature Distributions for Laser Powder Bed Fusion Processes," J. Res. Natl. Inst. Stan., 126, p. 126013.
[27] Lu, Yan, Zhuo Yang, Jaehyuk Kim, Hyunbo Cho, and Ho Yeung. "Camera-based coaxial melt pool monitoring data registration for laser powder bed fusion additive manufacturing." In ASME International Mechanical Engineering Congress and Exposition, vol. 84492, p. V02BT02A045. American Society of Mechanical Engineers, 2020.
[28] Lane, Brandon, and Ho Yeung. "Process monitoring dataset from the additive manufacturing metrology testbed (ammt): Overhang part x4." Journal of Research of the National Institute of Standards and Technology 125 (2020): 1-18.
[29] Yeung, Ho, Brandon M. Lane, M. A. Donmez, Jason C. Fox, and J. Neira. "Implementation of advanced laser control strategies for powder bed fusion systems." Procedia Manufacturing 26 (2018): 871-879.
[30] Ly, Sonny, Alexander M. Rubenchik, Saad A. Khairallah, Gabe Guss, and Manyalibo J. Matthews. "Metal vapor micro-jet controls material redistribution in laser powder bed fusion additive manufacturing." Scientific reports 7, no. 1 (2017): 1-12.
[31] Yang, Zhuo, Yan Lu, Brandon Lane, Jaehyuk Kim, Yande Ndiaye, and Sundar Krishnamruty. "Analyzing Remelting Conditions based on In-Situ Melt Pool Data Fusion for Overhang Building in Powder Bed Fusion Process." In 2021 International Solid Freeform Fabrication Symposium. University of Texas at Austin, 2021.
[32] Yang, Zhuo, Yan Lu, Simin Li, Jennifer Li, Yande Ndiaye, Hui Yang, and Sundar Krishnamurty. "In-Process Data Fusion for Process Monitoring and Control of Metal Additive Manufacturing." In International Design Engineering Technical Conferences and Computers and Information in Engineering Conference, vol. 85376, p. V002T02A072. American Society of Mechanical Engineers, 2021.